

1 Recommendations for seismic analysis of a molten salt reactor

2 Faizan Ul Haq Mir^{1*}, Andrew S. Whittaker², Benjamin D. Kosbab³, and Nam Nguyen⁴

3 ¹Post-doctoral Scholar, Department of Civil, Structural, and Environmental Engineering, University at Buffalo,
4 Buffalo, NY, USA

5 ²SUNY Distinguished Professor, Department of Civil, Structural, and Environmental Engineering, University at
6 Buffalo, Buffalo, NY, USA

7 ³Principal, Simpson Gumpertz & Heger, Atlanta, GA

8 ⁴Principal Engineer, Kairos Power, Alameda, CA

9 *Email for correspondence: faizanul@buffalo.edu

10

11 Abstract

12 A Fluoride-salt cooled High-temperature Reactor (FHR) that uses circulating solid pebbles, filled with
13 TRISO particles, as a fuel and positively buoyant graphite reflector blocks as moderator is at an advanced
14 stage of development. Seismic base isolation supports a pathway for cost competitive and rapid
15 deployment of this molten salt reactor (MSR) in regions of different seismic hazard. This paper presents
16 recommendations for analysis and modelling of different components of a base-isolated MSR, based on
17 results of earthquake-simulator tests on a scale model of the reactor. Recommendations are provided for
18 evaluating the sloshing behavior of the coolant in an annular region inside the reactor and for estimating
19 hydrodynamic loads for use in analysis of structural and mechanical components. Hydrodynamic loading
20 on the reflector blocks is discussed and a practical approach to estimate forces in the connections between
21 them is presented. Approaches for modelling and analysis of two 2D horizontal base-isolation systems,
22 utilizing spherical sliding bearings, are validated using results from experiments. The recommendations
23 apply to reactor vessels with similar fluid-structure systems.

24

25 **Keywords:** molten-salt reactor, annular tanks, base isolation, graphite reflector, seismic analysis

26

27 1. Introduction

28 To inform the seismic design of a base-isolated Fluoride salt-cooled High temperature Reactor (FHR),
29 which uses circulating solid pebbles, filled with TRISO (DOE 2019) particles, as the nuclear fuel, and
30 graphite blocks as a moderator, a set of earthquake-simulator experiments was executed on a scale model
31 of the reactor. The experiments, described in detail in Mir *et al.* (2022b) and summarized here, included
32 representations of safety-critical reactor components: water representing the molten salt (Flibe), an outer
33 vessel made of carbon steel, a concentric core barrel fabricated using aluminum, positively buoyant
34 polypropylene blocks representing the graphite moderator, and positively buoyant polypropylene
35 spherical pebbles representing fuel pebbles.

36 Mir *et al.* (2022b) describes scaling analysis for different test components of the model. The model
37 components were scaled using different governing scaling laws such that important component behaviors

were simulated as best as possible at the model scale. Figure 1a presents a schematic of the tested specimen. The outer vessel was a carbon steel cylinder, 2 m high and 1.52 m in diameter. An aluminum core barrel was installed inside the outer vessel and the two were separated by a 14.6 mm wide annulus that was sealed at the top using a rubber ring. This annular space is referred to as the *outer annulus* hereafter. The height of the core barrel was smaller than the outer vessel (see Figure 1a). A reflector-block assembly that comprised individual polypropylene blocks stacked on top of each other and connected using shear pins and keys was installed inside the core barrel. The assembly comprised sixteen vertical columns and a top block referred to hereafter as the *plug*. Each of the sixteen vertical columns comprised a stack of fourteen blocks, denoted RB-1 through RB-14 in Figure 1b. Blocks RB-1 and RB-14 denote the lower most and the upper most blocks in a column, respectively. The inner surface of the core barrel and the outer surface of the reflector block assembly were separated by 10 mm, referred to as the *inner annulus* here. Water was filled up to a height of 1.93 m and was free to slosh in the inner annulus. Sloshing in the outer annulus was prevented by the placement of a rubber ring. Spherical polypropylene pebbles, 15.87 mm in diameter and 285000 in number, were placed inside the reflector-block assembly. In the water-filled condition, the reflector-block assembly floated above the base of the vessel and was in contact with the head (see Figure 1a) of the vessel. An arrangement of steel pins was provided near the base and head of the vessel to restrict the lateral movement of the reflector-block assembly in the floating condition. The pins allowed for free sliding of the assembly in the vertical direction. (In the prototype reactor, the coolant flows down in the outer annulus and bottom up through the pebble bed for extraction of heat. In the model, this coolant flow was not simulated.) The head of the assembly was a 38.1 mm thick circular plate and was fabricated with through holes for bolts and slots for instrumentation wires and pebble loading and viewing. Two types of spherical sliding bearings (isolators in Figure 1a) were used to seismically base isolate the scale model: Single concave Friction Pendulum (SFP) and Triple Friction Pendulum (TFP).

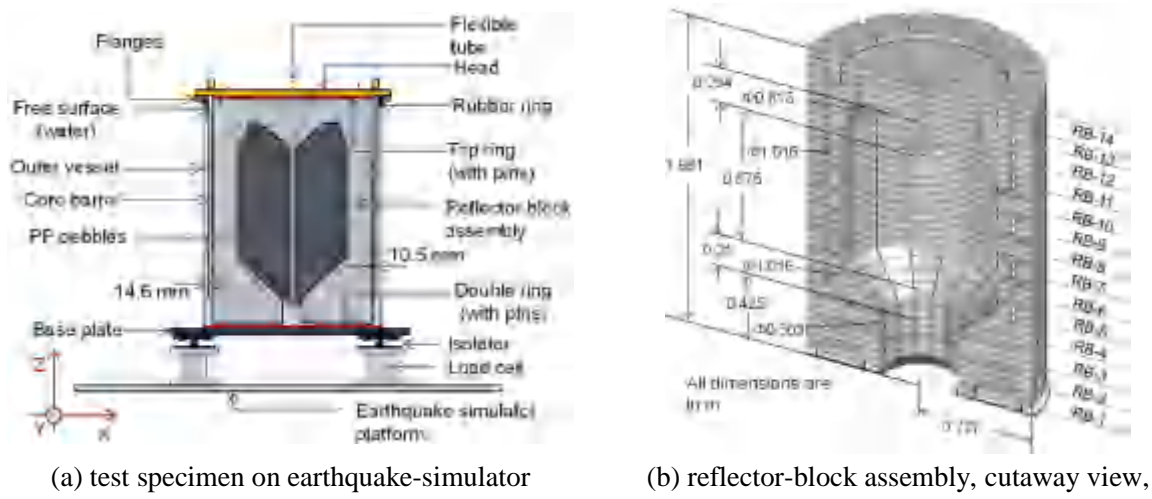


Figure 1. Test specimen in Mir et al. (2022b)

The instrumentation used in the experiments recorded the dynamic response of the fluid (hydrodynamic pressure and sloshing displacements in the inner annulus), base reactions, isolation system displacements,

dynamic responses of the vessel, core barrel, and reflector blocks, and pebble bed compaction under shaking. Traditional earthquake engineering instruments, load cells, accelerometers, and pressure gages, were used in tandem with borescopes and bespoke float-and-Temposonic gages (see Appendix B of Mir *et al.* (2022c)) to record the seismic response of the reactor components. Three recorded ground motions and one synthetic motion, all triplets, were used as seismic inputs. The recorded ground motions were from the 1999 Chi-Chi Earthquake, the 1940 Imperial Valley earthquake, and the 1952 Kern County earthquake, and were extracted from PEER Ground Motion Database (<http://ngawest2.berkeley.edu>). The synthetic triplet had frequency contents that spanned a broad range (< 50 Hz) and is referred to as the broad-band motion (BBM) hereafter. The recorded motions were time-scaled to be consistent with the length scale of test specimen: the time-axis was compressed by a factor of 1.6 (= $\sqrt{1/S_L}$, where $S_L = 0.39$ per Mir *et al.* (2022b)). Tests were conducted in the fixed-base and base-isolated configurations. Analysis of the test results, described in detail in Mir *et al.* (2022b), revealed the following:

1. The outer vessel, core barrel, and the reflector-block assembly responded as a near-rigid unit and accordingly, accurate estimates of base reactions can be computed using a lumped-mass model.
2. The damping associated with sloshing of fluid in the inner annulus was large (30% of critical). The time series of sloshing wave height could be recovered approximately using an analytical solution for sloshing responses in a regular cylindrical tank (see Veletsos (1984)) and a large value of damping.
3. The packing fraction of the pebble bed (i.e., ratio of volume of pebbles to the summation of the volume of pebbles and voids) changed by less than 3% after 150+ seconds of strong shaking; the percentage change varied as a function of the initial packing fraction.
4. The use of base isolation systems utilizing model-scale SFP and TFP bearings led to reductions in peak horizontal accelerations at the base of the outer vessel by factors between 1.2 and 4.6. The axial stiffness of the model-scale bearings used in the two isolations systems was *small* at the axial load developed in the tests and resulted in amplification in accelerations at high frequencies (25+ Hz) in the vertical and rocking directions.

Table 1. Earthquake-simulator inputs used for testing in Mir *et al.* (2022b)

Motion	Event	Recording station	Time scale compression	Peak accel. (g)		
				x	y	z
CCE [†]	Chi-Chi earthquake, 1999	TCU052	1.6	0.4	0.19	0.14
ECE	Imperial Valley earthquake, 1940	El Centro Array #9	1.6	0.4	0.3	0.25
KCE	Kern County earthquake, 1952	Taft Lincoln School, 21	1.6	0.57	0.65	0.39
BBM	-	-	-	0.37	0.22	0.23

[†]In base-isolated tests, the amplitudes of the three components of the CCE motion were reduced to 80% of the values reported here. The reduced amplitude CCE motion is referred as CCE-R hereafter.

This paper presents recommendations for analysis and modelling of different components of a base-isolated MSR, based on results of tests described in Mir *et al.* (2022b). The focus of the following sections is on modelling fluid behavior to compute sloshing wave height and hydrodynamic pressure, estimation of forces in connections between blocks in a reflector assembly, and numerical analysis of the two base-isolation systems used in the physical tests.

96 **2. Fluid behavior**

97 **2.1 Sloshing responses in small-width annuli**

98 Mir *et al.* (2022b) demonstrated that reasonably accurate estimates of sloshing wave height in the inner
99 annulus could be obtained using an analytical solution for sloshing responses in a *regular cylindrical tank*
100 (see Veletsos (1984)). The key inputs required for the analytical solution include the height of fluid in the
101 *regular cylindrical tank*, radius of the *regular cylindrical tank*, and the damping ratio in sloshing modes.
102 These were set equal to the distance between the underside of the reflector-block assembly and the base
103 of the vessel in the tests, the radius of the core barrel, and 30% of critical, respectively. The damping ratio
104 of 30% was calibrated using data from the experiments.

105 Numerical estimation of sloshing responses in the inner annulus is challenging for two reasons: 1) a
106 computationally expensive (fine) finite element mesh is required in the annulus to obtain meaningful
107 results for wave height, and 2) the computation of the damping ratio in the sloshing mode, associated with
108 boundary effects in the thin annulus and constricted flow between gaps in reflector blocks, is fluid- and
109 geometry-specific.

110 To address the challenge of computational expense, two annular tank geometries were modelled using the
111 Arbitrary Lagrangian Eulerian (ALE) solver of LS-DYNA (LSTC 2017): 1) model A, the benchmark,
112 with a large annulus, with a ratio (k) of inner tank radius to outer tank radius of 0.5, and 2) model B with a
113 small (thin) annulus, with $k = 0.98$. The width of the annulus in the second model was set nearly equal to
114 that of the inner annulus in the test specimen. The radius of the outer tank in model A and model B was
115 equal to that of the core barrel in the test specimen. Figure 2 shows the two finite element models and the
116 used Cartesian and cylindrical coordinate systems.



117 **Figure 2. Annular tanks analyzed in LS-DYNA, cutaway and plan views, dimensions in m**

118 The outer tank, inner tank, and the base of each annular tank, shown in green in Figure 2, were modeled
119 using Lagrangian, four-node, shell elements, and as a rigid material such that their mass was nearly zero.
120 (Acceleration cannot be applied to an element(s) with zero mass in LS-DYNA.) The fluid (water) domain
121 and the space above the free surface (to accommodate sloshing), shown in blue and gray, respectively, in
122 Figure 2, were modeled using Eulerian, eight-node solid elements. These Eulerian elements do not
123 deform but rather serve as a grid through which fluid can flow. The material properties of the fluid
124 domain were assigned using the *MAT (material) and *EOS (equation of state) cards in LS-DYNA.
125 Water was assigned a density of 1000 kg/m^3 , a dynamic viscosity of 0 Ns/m^2 , and a bulk modulus of 2.2

126 GPa, to simulate inviscid and incompressible properties per Yu and Whittaker (2022). The space above
 127 the water was assigned *void properties* using the *INITIAL_VOID card. The fluid-domain elements near
 128 the walls of the inner and the outer tanks in model A were smaller than elsewhere (see plan view in Figure
 129 2a). The annular space in model B was meshed using four elements in plan (see Figure 2b). Solid
 130 elements in the fluid domain (including the *void space*) shared nodes with the structural shell elements.
 131 The vertical movement of the free surface (sloshing) under seismic inputs was tracked by defining
 132 massless nodes, referred to as *tracers*, on the free surface of water using the *DATABASE_TRACER
 133 card. A detailed discussion on *tracers* is presented in Yu and Whittaker (2021).

134 Both models were analyzed for a horizontal input of four cycles of a sinusoid with a frequency of 1 Hz
 135 and an amplitude of 0.1g. The acceleration history was input using the keyword
 136 BOUNDARY_PRESCRIBED_MOTION_RIGID. An acceleration of 9.81 m/s^2 was applied in the
 137 negative z direction in the models to simulate gravity. This acceleration was applied as a ramp from 0 to
 138 9.81 m/s^2 in the initial 0.2 s of analysis, followed by a constant gravitational acceleration of 9.81 m/s^2
 139 thereafter. Horizontal acceleration inputs to the models were applied after the initial 1 s of analysis. This
 140 ensured proper initialization and stabilization of hydrostatic pressure in the models before the application
 141 of the horizontal acceleration input.

142 The hydrodynamic pressure on the outer tank wall and the wave height (surface displacement) responses
 143 extracted from the numerical analysis of models A and B were compared with predictions using the
 144 analytical solution for hydrodynamic responses in annular tanks by Tang *et al.* (2010). (The analytical
 145 solution assumes an incompressible, inviscid fluid, similar to the fluid material definition used in models
 146 A and B.) For model A, the pressure histories near the base and the wave height histories at a point 10
 147 mm from the outer tank wall were in close agreement: see Figure 3a and Figure 3b, respectively. (Errors
 148 in maximum values are indicated on plots as ϵ .) The numerically predicted wave height history 4 mm
 149 from the outer tank wall, shown in Figure 3c, does not agree with the analytical prediction.

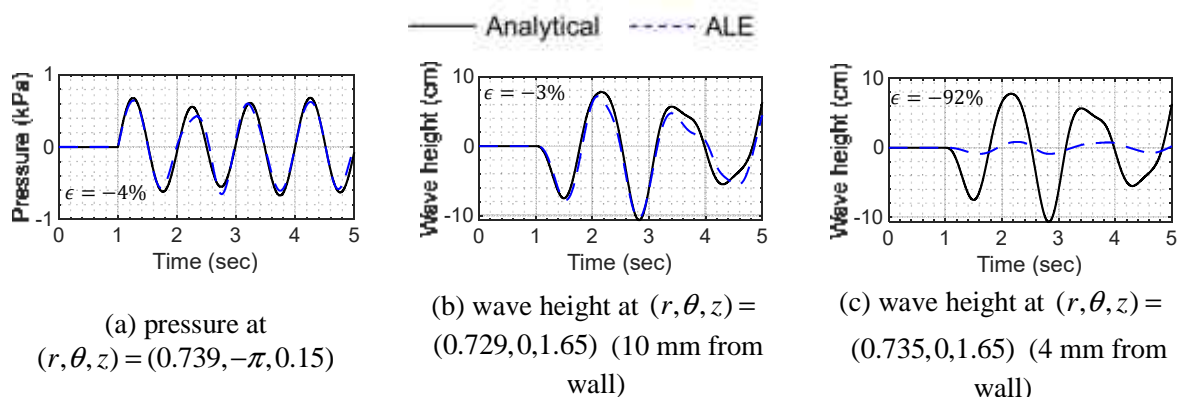


Figure 3. Model A, ALE results and analytical predictions, sinusoidal input, coordinates in m, errors (ϵ) in maximum values indicated

150
 151 The differences between the analytical and numerical predictions for wave height close to the wall of the
 152 tank are a result of boundary effects: the vertical fluid velocity at the tank wall is zero because the fluid

153 and shell elements at the boundary share common nodes, and waves do not form correctly; see Yu and
 154 Whittaker (2022) for details.

155 Results of analysis of model B are presented in Figure 4 and Figure 5. Pressure histories at three heights
 156 along the wall (Figure 4) and wave height histories at two distances from the wall (Figure 5) are plotted.
 157 The plots presented in Figure 4 show that the numerical (ALE) results for hydrodynamic pressure are in
 158 reasonable agreement with the analytical predictions. Reasonably accurate estimates of wave height are
 159 obtained at a point 6 mm from the outer wall (see Figure 5a). However, similar to model A, the numerical
 160 predictions of wave height closer to the wall are inaccurate (see Figure 5b). To investigate whether
 161 analysis of a finer mesh would improve the numerical predictions of wave height near the edges of the
 162 annulus, model B was re-analyzed with element sizes reduced by a factor of 2. (In the original model B,
 163 four fluid elements were used along the radial direction in the annulus. In the model with a refined mesh,
 164 eight elements were used.) Results from model B with the refined mesh are shown in Figure 6 and Figure
 165 7: the numerically predicted hydrodynamic pressure histories do not improve with mesh refinement (see
 166 Figure 6), although the numerically predicted wave-height history close to the wall improves. The mesh
 167 refinement was computationally expensive and led to a thirteen-fold increase in simulation run time. This
 168 is of significance for numerical simulation of sloshing responses in the small annular space in the MSR
 169 (and reactor vessels with similar internal construction). An important outcome from the numerical
 170 analysis of model B, used in the next section, is that the hydrodynamic pressure time series along the tank
 171 wall in the small annulus are predicted accurately, even though the wave height time series may not be
 172 predicted with the same fidelity across the width of the annulus.

173 The ALE solver was used to identify computational challenges in the estimation of sloshing responses in
 174 thin annular spaces. (The computational cost associated with other solvers in different finite element
 175 packages will almost certainly be different. And there are solvers (e.g., ICFD in LS-DYNA) that provide
 176 other options for modeling the interface between fluid and solid domains.) However, if computational
 177 expense is considered in conjunction with the challenges of defining damping in the sloshing modes
 178 accounting for boundary effects and flow between gaps, it would appear to be more reasonable (and
 179 practical) to use the regular tank approximation of Mir et al. (2022b) to estimate wave height in the inner
 180 annulus of the reactor.

181

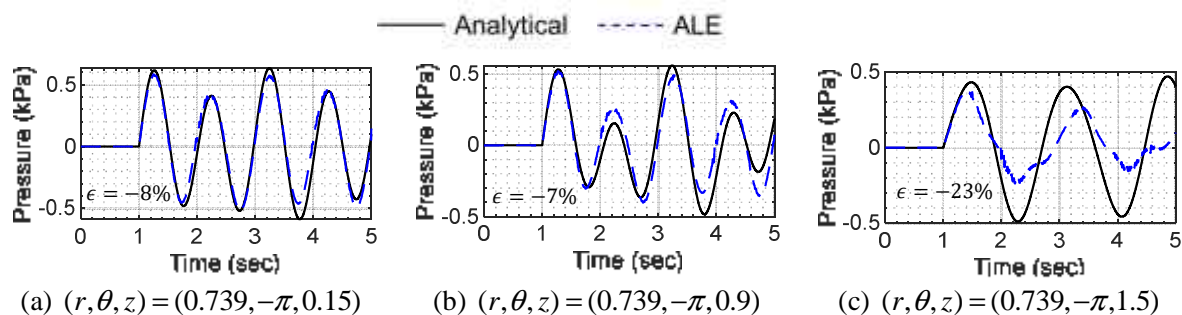


Figure 4. Model B, ALE results and analytical predictions for hydrodynamic pressure at three locations, sinusoidal input, coordinates in m, errors (ϵ) in maximum values indicated

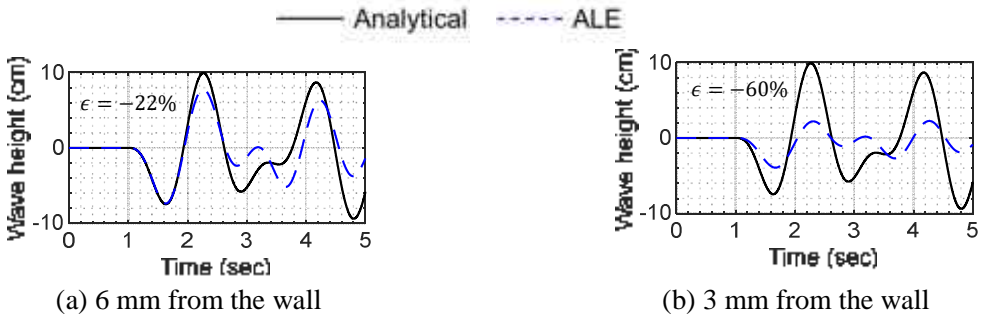


Figure 5. Model B, ALE results and analytical predictions for wave height at two distances from the outer wall, sinusoidal input, errors (ϵ) in maximum values indicated

182

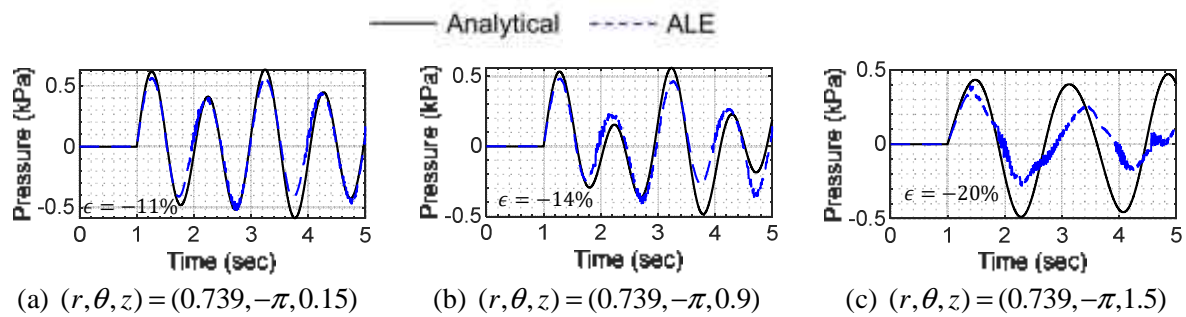


Figure 6. Model B with finer mesh, ALE results and analytical predictions for hydrodynamic pressure at three locations, sinusoidal input, coordinates in m, errors (ϵ) in maximum values indicated

183

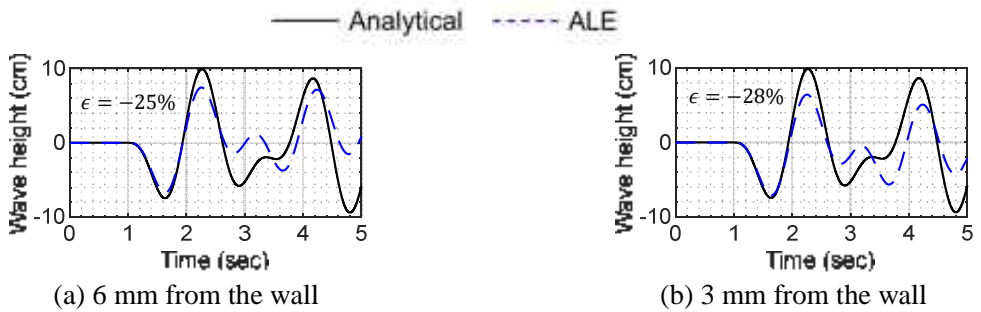


Figure 7. Model B with finer mesh, ALE results and analytical predictions for wave height at two distances from the outer wall, sinusoidal input, errors (ϵ) in maximum values indicated

184

185 2.2 Estimation of hydrodynamic loads

186 Hydrodynamic pressure loadings are needed for the analysis of reactor components (e.g., vessel, core
187 barrel). The hydrodynamic pressure loads would be calculated most precisely by analysis of finite
188 element models that involve an explicit representation of the fluid, contact between reflector blocks, and
189 gap elements between the core barrel and vessel. Such detailed models are computationally intractable

190 currently. A practical solution is to de-couple the fluid and solid domains and use 1) a *fluid-only* model
191 for estimating hydrodynamic pressure loads, and subsequently, 2) the calculated pressure histories for
192 analysis of models of the structural and mechanical components. This approach is robust because the
193 structural (solid domain) components of the model, including the vessel, core barrel, and reflector blocks,
194 responded as a unit during earthquake shaking.

195 The efficacy of using a *fluid-only* model for estimation of hydrodynamic pressure histories was assessed
196 using a *double-annulus* ALE model representative of the fluid-domain geometry in the test specimen. The
197 *double-annulus* model, shown in Figure 8, considered the core barrel, the outer vessel, and the reflector-
198 block assembly as rigid boundaries around (inside; in case of the core barrel) the fluid domain. These
199 boundaries are shown in grey in Figure 8. The geometry of the lower surface of the reflector-block
200 assembly (see Figure 1a) was simplified for this modelling exercise and the fluid-domain inside the
201 reflector-block assembly was not modelled. The fluid domain is shown in blue in Figure 8. The core
202 barrel partially separated the fluid domain into two annuli. Sloshing was restrained in the outer annulus
203 but permitted in the inner annulus. Accordingly, *void space* was modelled above the fluid domain in the
204 inner annulus, as shown in light grey in Figure 8. Like model B described in the previous section, four
205 solid elements were used across the width of the inner annulus. The model definition was like that
206 described earlier, except that the fluid was assigned a dynamic viscosity of 10^{-6} Ns/m², representative of
207 the water used in the experiments.

208 The *double-annulus* model was subjected to accelerations recorded at the base of the test specimen in
209 tests with two unidirectional (x) inputs: CCE and KCE motions with amplitudes of 0.4g and 0.57g per
210 Table 1. The resulting numerical hydrodynamic pressure histories at three locations on the wall of the
211 outer vessel (PW1, PW2, and PW3 in Figure 8) were compared with pressure gage data at the same
212 locations on the outer vessel in the test specimen. The pressure gages in the test specimen at these
213 locations are named similarly: PW1, PW2, and PW3. Data from PW2 and PW3 characterize the behavior
214 of the fluid in the outer annulus. The pressure gage PW1 was located below the lower end of the core
215 barrel and was thus *common* to the outer and the inner annuli. In addition to comparing hydrodynamic
216 pressure time series, the wave height recorded in tests in the inner annulus was compared with
217 numerically obtained wave height time series at the center of the annulus at a location corresponding to
218 that of a wave height measuring sensor in the experiments. Figure 9 and Figure 10 present results for the
219 two 1D motions. The differences in peak experimental and numerical responses are noted on the plots in
220 Figure 9 and Figure 10 as ε .

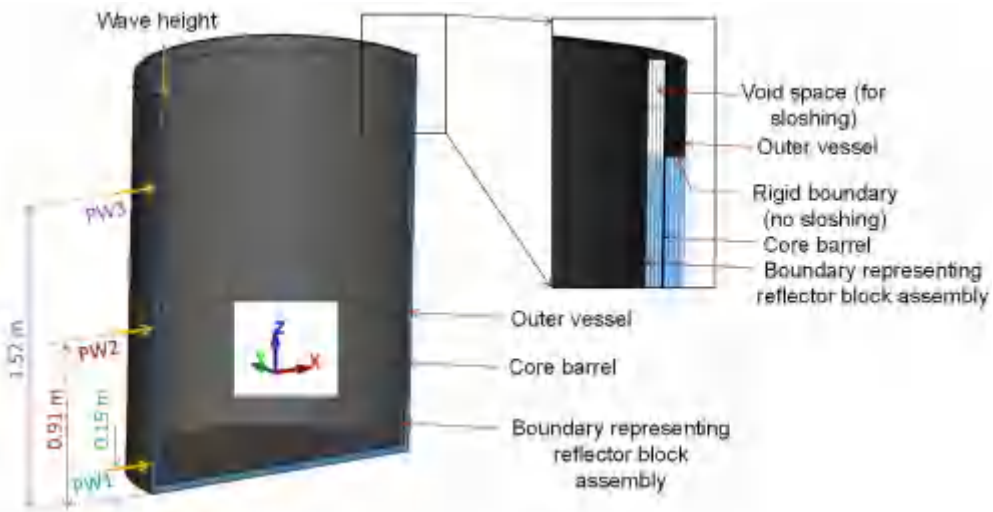


Figure 8. Cutaway view of the double-annulus model for estimating hydrodynamic pressure, LS-DYNA,

221 Notably, the numerical and experimental pressure time series at the three locations are in good agreement
 222 (see Figure 9a, b, and c and Figure 10a, b, and c). The predicted and measured wave height time series
 223 (see Figure 9d and Figure 10d) are substantially different in terms of both peak values and time variation,
 224 with possible reasons including:

- 225 1. The damping related to wave action in the numerical model, which results from the definition of
 226 fluid viscosity and a small value of the hourglass-control-related coefficient, does not address the
 227 dissipation of energy due to flow between the gaps in the reflector blocks and in the narrow
 228 annulus.
- 229 2. The method for outputting wave height currently employed in the ALE solver of LS-DYNA is
 230 not robust: the tracers are not stationary in plan but rather move with the fluid (Yu and Whittaker
 231 2021).
- 232 3. The breaking of waves in the annulus (see Figure 11) can neither be measured because there is no
 233 smooth free surface nor predicted with an ALE-type solver.

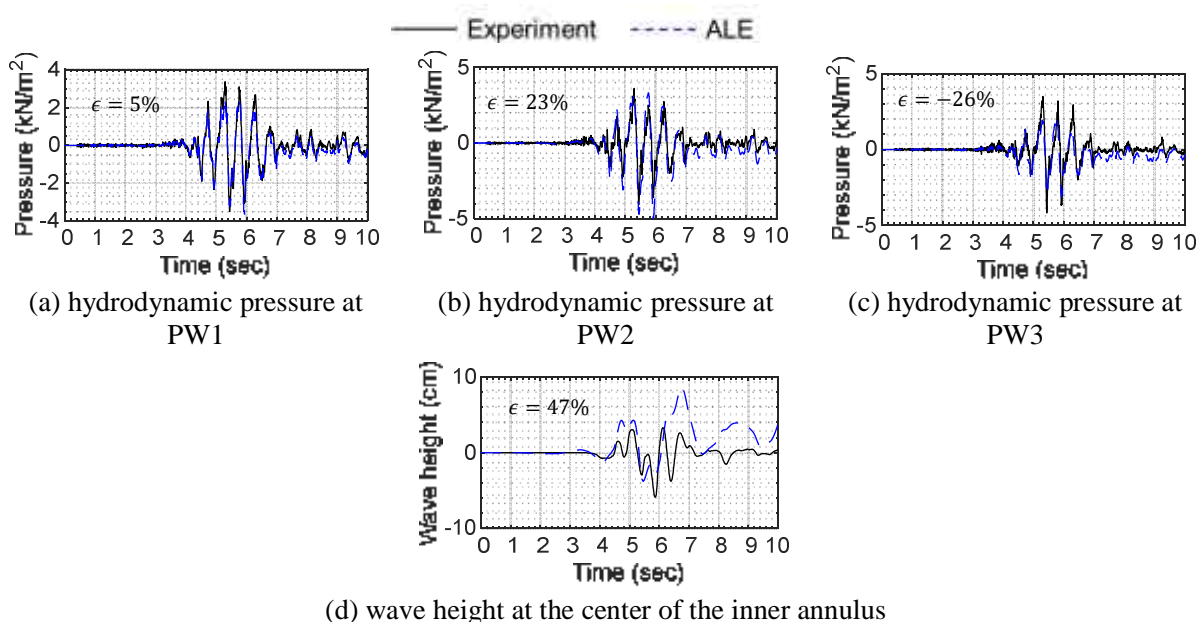
234 Like the observations made in the previous section, inaccuracies in the numerically predicted wave height
 235 histories do not translate into similar discrepancies in pressure responses on the boundary of the annulus.
 236 The pressure histories close to the base of the annulus are predicted more accurately than those near the
 237 top. Accordingly, and with little conservatism, an analyst could choose to use the pressure histories
 238 obtained at the base and mid-height of the double annulus model and extrapolate the latter to the top of
 239 the annulus.

240
 241
 242
 243

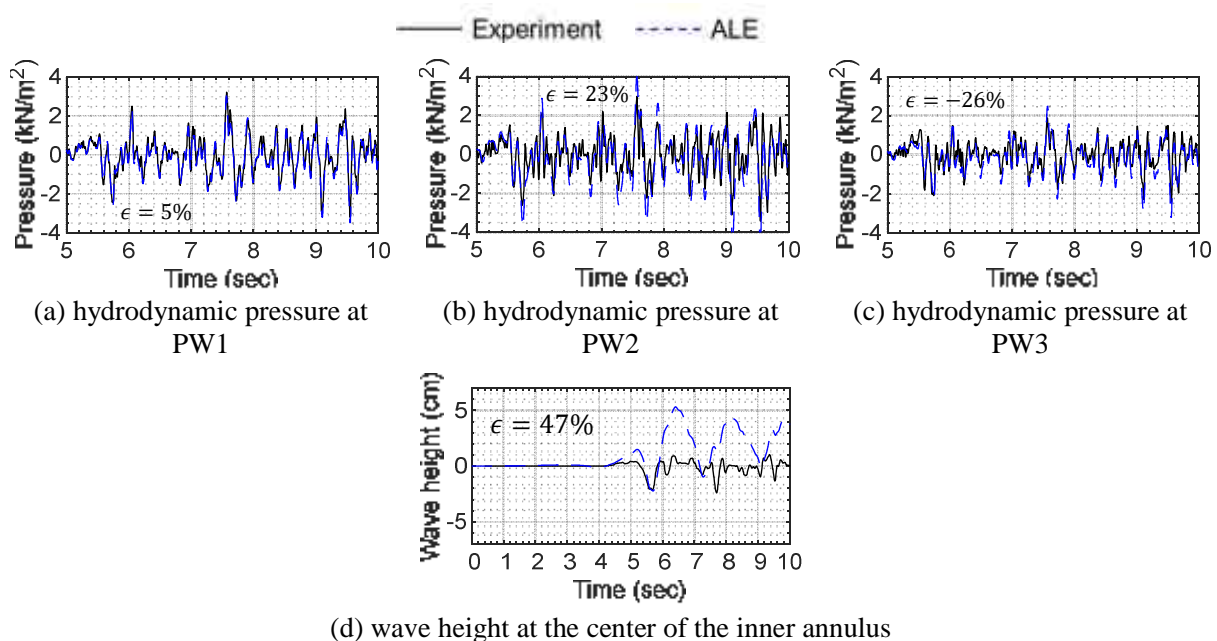
244

245

246

**Figure 9. Numerical and experimental results, double-annulus model, 1D CCE motion per Table 1.**

247

**Figure 10. Numerical and experimental results, double-annulus model, 1D KCE motion per Table 1.**

248

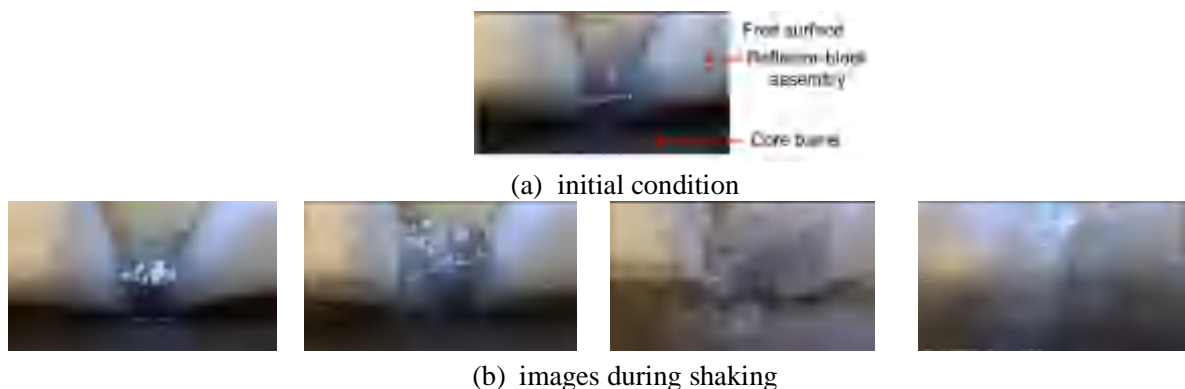


Figure 11. Wave breaking in the annulus, 3D CCE motion

249

250 3. Estimating forces in the reflector-block assembly

251 This section provides a pathway to compute earthquake-induced forces in the pins and keys that join
 252 blocks in a reflector assembly, based in part on observations from the experiments described in Mir *et al.*
 253 (2022b), and numerical analysis. Horizontal and vertical shaking are addressed in the following sub-
 254 sections.

255 3.1 Forces in pins and shear keys due to horizontal earthquake shaking

256 Blocks in the reflector assembly introduced earlier are joined by cylindrical pins and cuboidal shear keys
 257 made of polypropylene: pins and shear keys hereafter. Figure 12a presents the locations of the pins and
 258 shear keys in a layer of reflector blocks in the test specimen. Figure 12b and Figure 12c presents the
 259 dimensions of the shear keys and pins, respectively. The shear keys were installed in the orientation of
 260 Figure 12a. The shear keys connect adjacent blocks in a layer and adjacent layers of blocks, and reduce
 261 fluid flow (or core bypass flow in the prototype reactor) between adjacent columns of blocks. Each key
 262 resists shearing forces along two planes identified as planes A1 and B in Figure 12b. The pins were used
 263 primarily to align blocks in adjacent layers but resist shearing forces through their cross section (plane A2
 264 per Figure 12c). The shear strengths of the keys and pins along planes A1, B, and A2 per Figure 12b, c
 265 are 35 kN, 100 kN, and 3.4 kN, respectively, calculated as 0.577 times the assumed tensile strength of
 266 polypropylene (= 27 MPa): the von Mises criterion.

267

268

269

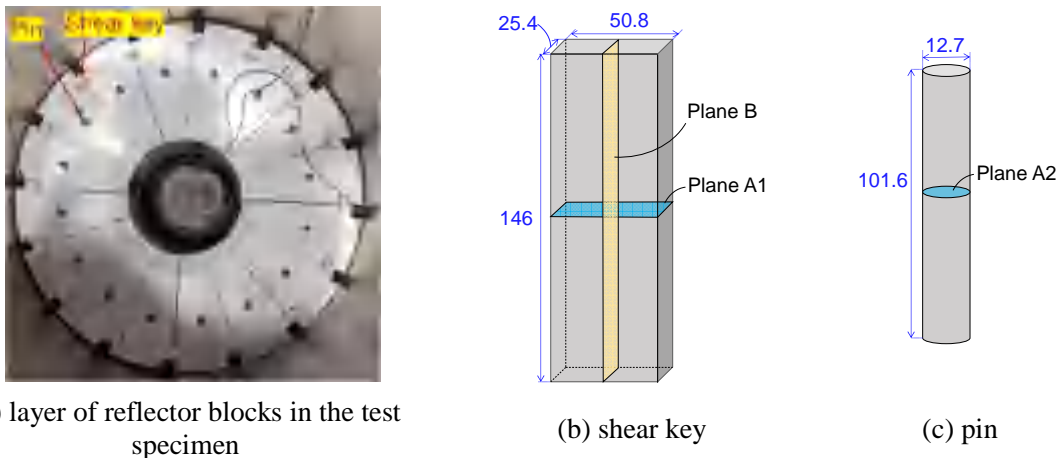


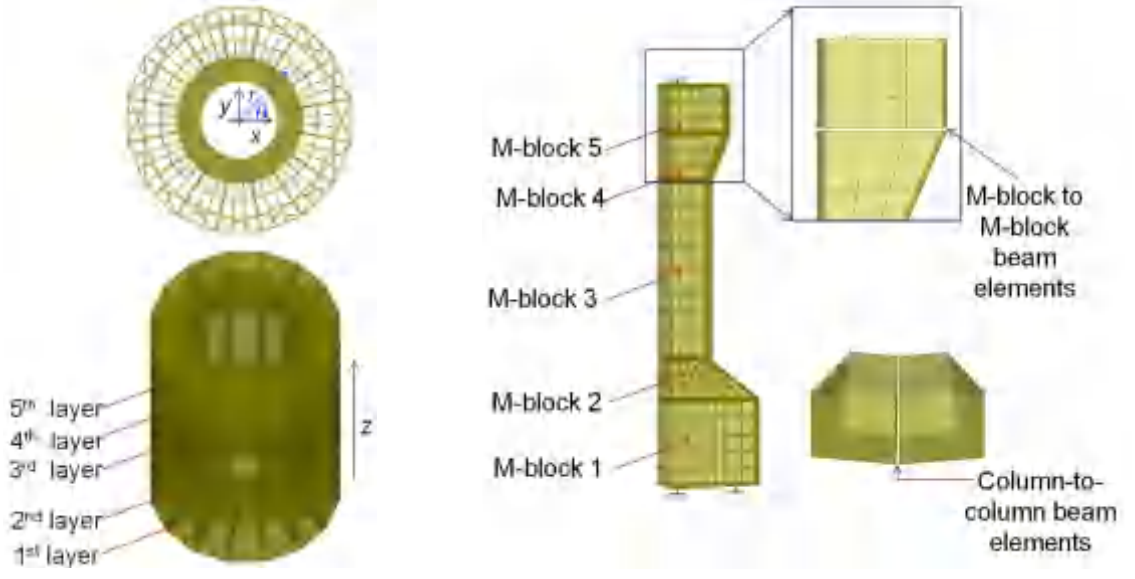
Figure 12. Shear keys and pins installed in reflector-block assembly, planes resisting shear forces, dimensions in mm

270
 271 A simplified finite element model of the reflector-block assembly, presented in Figure 13, was
 272 constructed in SAP2000 (CSI 2017). The model comprised sixteen individual columns. Each column was
 273 modelled using five *master blocks* (referred as M-blocks hereafter), as shown in Figure 13, rather than the
 274 fourteen blocks in each column of the test specimen. Accordingly, the finite element model comprised
 275 five layers of master blocks (see Figure 13a). The five master blocks were chosen to mimic the shape of
 276 an individual column in the test specimen. Each M-block comprised a set of massless rigid beams (to
 277 track edges) and rigid area elements. The area elements were assigned *area masses* such that the mass of
 278 an M-block in the model equaled the mass of the group of test blocks it represented: for example, the
 279 mass of M-block 3 per Figure 13 was equal to the mass of blocks RB-5 through RB-10 per Figure 1b. The
 280 total mass of the reflector assembly in the model was 1900 kg. The mass of the pebbles and water inside
 281 the reflector-block assembly (1000 kg) was distributed as an area mass on the inner area elements of M-
 282 blocks 1 through 4 in each column.¹ Similarly, the mass of the plug was equally distributed to the inner
 283 area elements of M-block 5 in each of the sixteen columns. Each connection between adjacent M-blocks,
 284 in a layer or a column, was modelled using four beam elements. The beams were modelled using a stiff
 285 elastic material to ensure that the modal frequencies of the assembly were very high (> 300 Hz, the
 286 assembly was effectively rigid).² The pins at the top and bottom (one per block at the top and two per
 287 block at the bottom, per the geometry described in Mir *et al.* (2022b)) of each column of blocks were
 288 fixed against rotation and translation, as shown in Figure 13b. Horizontal (H) section cuts were made
 289 between the five layers of the M-blocks: H1 through H4 in Figure 14. Vertical, radial (R) section cuts
 290 were made between adjacent M-blocks in layer 3: R1 through R16 in Figure 14. Forces were output at

¹ The fluid-pebble mixture inside the core of the reflector block assembly is confined such that the hydrodynamic effects are purely impulsive. Modeling the fluid-pebble mixture as a distributed mass on the inside face of the reflector-block assembly is most reasonable.

²The frictional contact between blocks is ignored here, resulting in conservative (high) estimates of forces in the shear pins and keys. The beam elements in the numerical model functionally represent the pins and the keys in the physical model, but their primary purpose was to enable extraction of forces at block-to-block interfaces.

291 these section cuts. Additional horizontal section cuts, S1 through S16 were defined at the level of section
 292 cut H3 (see Figure 14) to output horizontal forces at the sixteen interfaces between M-blocks 3 and 4.



(a) SAP model and coordinate systems (b) one column of five blocks and connecting beam elements

Figure 13. Model of the reflector-block assembly in SAP2000

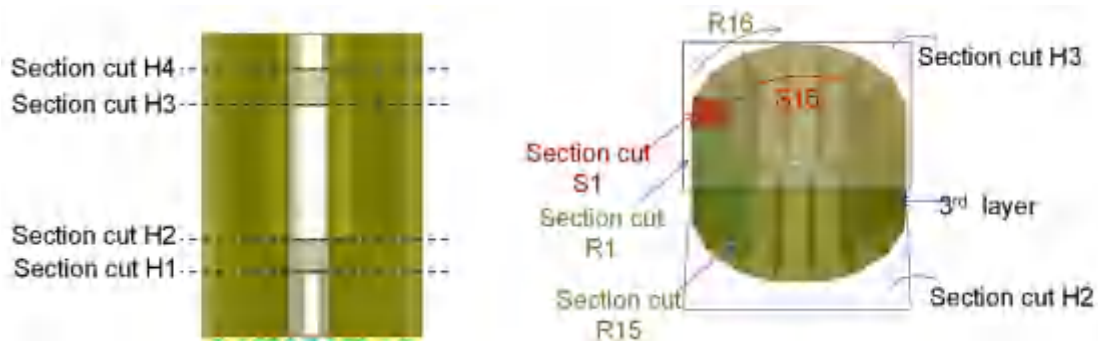


Figure 14. Section cuts defined in the model

293
 294 To quantify seismic demands in the pins and shear keys, which were not measured in the physical
 295 experiments, a simplified loading environment involving a dynamic acceleration of 1g was input to the
 296 model along the x direction. Forces were output using the section cuts identified above. Figure 15 presents
 297 the orientations of the forces output on different section cuts for the one directional input; the orientations
 298 are defined per the coordinate systems introduced in Figure 13a. The in-plane forces recorded on section
 299 cuts H1 through H4 only had components along the excitation direction (as expected) whereas forces
 300 recorded on other section cuts had components in both in-plane directions, as indicated in Figures 14b and
 301 14c.



(a) section cut H1 (through H4) (b) section cut R1 (through R16) (c) section cut S1 (through S16)

Figure 15. Orientation of in-plane forces output using section cuts (see Figure 14), one directional input, forces are denoted by the letter F and a subscript indicating direction, r is radial

302

303 Figure 16a presents the variation of total horizontal *shear* force along the height of the assembly, output
 304 using section cuts H1 through H4. The net inertial force associated with the 1 g horizontal acceleration of
 305 the model was 29 kN. The difference between the reactions at the top (13 kN) and bottom (16 kN) is due
 306 to the higher degree of restraint at the bottom (two pins per column) than at the top (one pin per column).
 307 (The reactions at the top and bottom were verified to be equal for a model with two pins per column at the
 308 top and bottom of the reflector-block assembly.) In the test specimen, the horizontal shear force at an H
 309 section cut is resisted by sixteen shear keys and sixteen pins along planes A1 and A2, respectively, per
 310 Figure 12 (assuming no frictional contact). The distribution of the shear force in the keys and pins of the
 311 sixteen columns is addressed later in this section. The horizontal shear force in a single column is resisted
 312 by one shear key and one pin (planes A1 and A2 per Figure 12).

313 The magnitudes of the resultant in-plane forces on section cuts R1 through R16 (in layer 3) are presented
 314 in Figure 16b: the forces are maximized at the section cuts that are aligned with the excitation direction
 315 (x ; 0, 180 degrees in Figure 16b) and minimized at the cuts nearly perpendicular to the excitation
 316 direction (90, 270 degrees in Figure 16b). Note that a single M-block in layer 3 of the finite element
 317 model represents six reflector blocks (RB-5 through RB-10 per Figure 1b) of the test specimen.
 318 Accordingly, the force on an R section cut in the model is distributed to six shear keys, each resisting
 319 force along plane B per Figure 12b. The maximum resultant force at an R section cut per Figure 16b for
 320 the constant acceleration input of 1g is 0.5 kN, which is three orders of magnitude smaller than the shear
 321 strength of the six keys, resisting force along plane B ($= 6 \times 100$ kN).

322 Figure 16c presents the magnitudes of the resultant in-plane forces on section cuts S1 through S16,
 323 located at section cut H3. The vector sum of forces on the sixteen section cuts (S1 through S16) is equal
 324 to the x -direction force on section cut H3 ($= 6.7$ kN; see Figure 16a): an expected outcome. The resultant
 325 of the y -direction forces (F_y per Figure 15c) on section cuts S1 through S16 is zero: another expected
 326 outcome. Note that the force on an individual section cut (e.g., S3) has components in both in-plane
 327 directions (F_x and F_y per Figure 15c). The curve presented in Figure 16c indicates that the shear force at
 328 a horizontal section in the reflector-block assembly (e.g., H3) is not distributed equally to the sixteen
 329 columns. Rather, columns aligned with the excitation direction (0, 180 degrees in Figure 16c) resist a

330 smaller shear force than those orthogonal to the excitation direction (90, 270 degrees in Figure 16c).³ As
 331 noted previously, the force on an S section cut is resisted by a shear key and a pin in the test specimen,
 332 along planes A1 and A2, respectively, per Figure 12b, c. Thus, the capacity of an S section cut in shear is
 333 38 kN (shear key along plane A1 = 35 kN and pin along plane A2 = 3.4 kN). Per Figure 16c, the
 334 maximum shear force on an S section cut is 0.52 kN for the constant acceleration input of 1g, which is
 335 approximately two orders of magnitude smaller than the capacity of 38 kN.

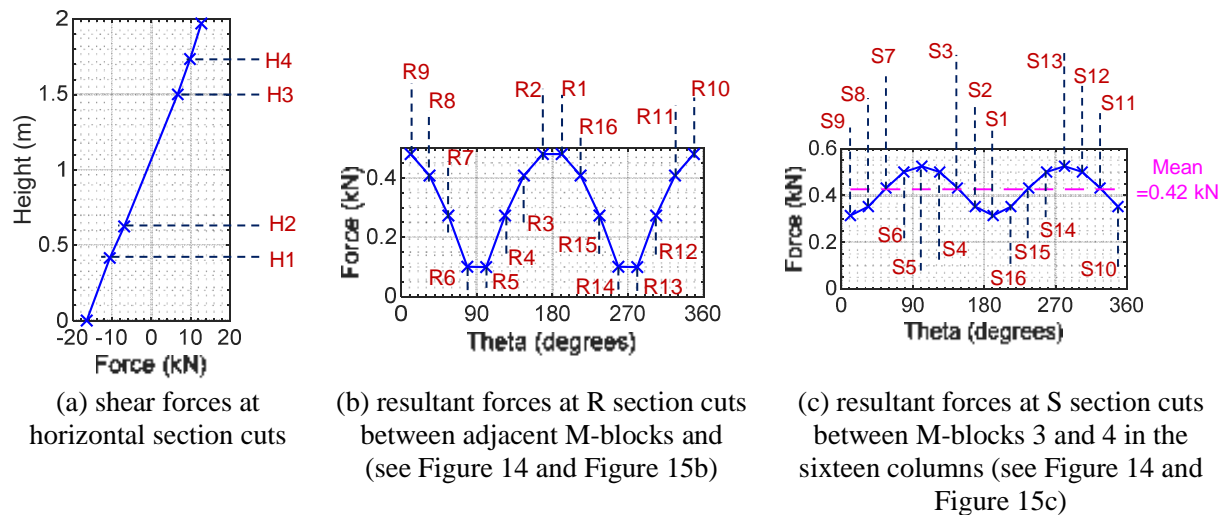


Figure 16. Section cut forces for 1g horizontal input

336
 337 The discussion presented above indicates that for the 1g horizontal input, the calculated force
 338 demands along R and S section cuts are orders of magnitude smaller than the shear capacity of the keys
 339 and the pins used in the test specimen. Since the model is linear and practically *rigid*, the distribution of
 340 forces along the H, R, and S section cuts for any earthquake input can be obtained by scaling the
 341 distributions presented in Figure 16 for the 1g horizontal input. Such scaling requires multiplying the
 342 forces presented in Figure 16 by the peak acceleration (in g) of the earthquake input to the vessel. (Note
 343 that the method of analysis described here does not consider tolerances (gaps) between the shear keys and
 344 pins and the corresponding slots machined in the reflector blocks. Tolerances will affect the number of
 345 shear keys and pins engaged in resisting forces, but this cannot be predicted. Importantly, the tolerances
 346 used to machine the plastic parts for the reflector block in the model are equal or similar to those planned
 347 for the graphite in the prototype reactor.)

348 The model described above does not consider the pressure loading on the outer surface of the reflector-
 349 block assembly due to the horizontal input acceleration. An approach to consider the pressure loading
 350 would be to extract the pressure histories on the surface representing the reflector-block assembly in the
 351 *double-annulus* model, described previously, and apply those at corresponding points in the described
 352 reflector-block assembly model or, simply extract the pressure history at one location (say near PW1 in
 353 Figure 8), ignore the variation of pressure along the height of the assembly, and use a $\cos\theta$ -type variation

³A useful analogy is here is the distribution of shear stresses along the cross-sectional depth in a prismatic circular beam: the stress is maximized near the neutral axis (mid-depth) and minimized at the top and bottom.

of pressure loading along the circumference. However, inclusion of pressure loading on the surface of the reflector-block assembly would lead to smaller design forces (at interfaces of layers/columns) than the case where the lateral pressure loading is ignored. This is because the direction of the net hydrodynamic load on the reflector-block assembly for a lateral input is such that it relieves the supports of the reflector-block assembly (and consequently, the pins and keys between blocks). Thus, analysis for lateral accelerations without pressure loading on the lateral surface of the reflector assembly will result in higher estimates of force.

3.2 Tri-directional shaking of the reflector-block assembly

Figure 17 presents fluid pressure loading profiles on the lateral and bottom surfaces of the reflector-block assembly in the presence of horizontal and vertical seismic inputs: the reflector-block assembly, shown in grey, is subjected to a horizontal (a_x) and a vertical (a_z) acceleration shaking. The acceleration due to gravity (g) acts in the negative z direction per the coordinate system shown in the figure.

The acceleration due to gravity (g) results in the hydrostatic pressure profiles $P_l(g)$ and $P_b(g)$ on the lateral surface and the base of the assembly, respectively, as drawn in the figure. (Subscripts l and b denote lateral and base, respectively.) Pressure loading profiles due to the vertical acceleration input (a_z) are similar to those due to g and are denoted $P_l(a_z)$ and $P_b(a_z)$ in Figure 17. The pressure loading profiles due to the horizontal acceleration input (a_x), denoted $P_l(a_x)$ and $P_b(a_x)$, can be estimated using the *double annulus* model described earlier, and each has a $\cos\theta$ -type variation around the circumference of the assembly. All pressure loadings on the vertical cylindrical surface can be ignored: $P_l(g)$ and $P_l(a_z)$ because they sum to zero net resultant force on the assembly, and $P_l(a_x)$ for the reason given at the end of Section 3.1.

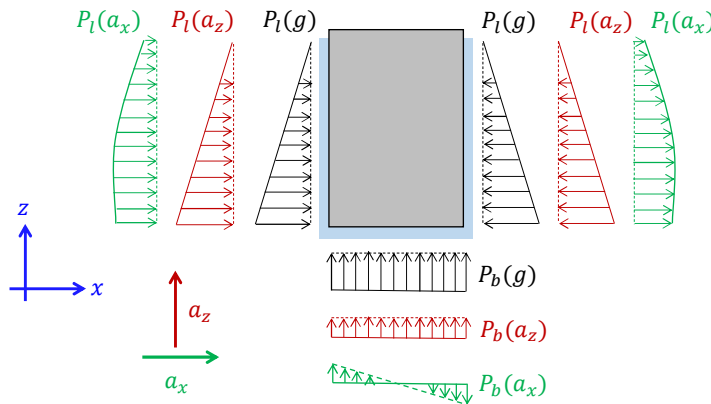


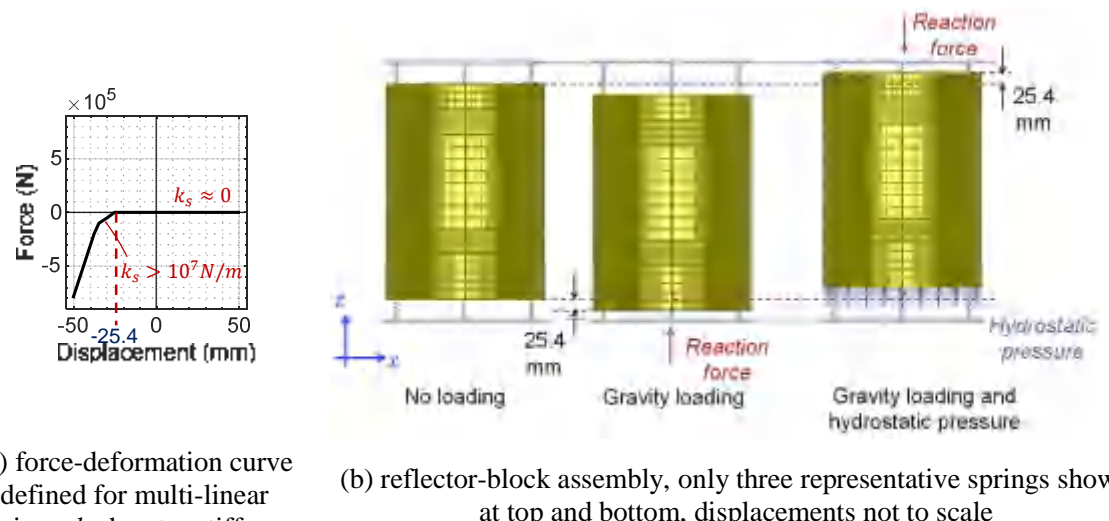
Figure 17. Fluid pressure loading profiles on the reflector-block assembly in the presence of vertical and lateral acceleration inputs

The SAP2000 finite element model described in the previous section was modified for analysis involving three-dimensional seismic inputs. The axial restraints at support points at the top and bottom of each column were replaced by multi-linear springs to accommodate vertical movement of the reflector-block assembly under fluid loading. The axial force-deformation curve for the springs was such that they were

effectively rigid in compression for a displacement greater than 25.4 mm and had a near-zero stiffness for smaller displacements in compression and for all displacements in tension; see Figure 18a.

Figure 18b presents the state of the reflector-block assembly in the finite element model under no loading, gravity loading, and gravity and hydrostatic loading. Under gravity loading only, the springs at the base are compressed and carry the weight of the assembly ($= 29 \text{ kN}$), and the springs at the top are in tension and provide negligible resistance ($k_s \approx 0$ in tension). An upward pressure is applied at the base of the assembly to simulate hydrostatic pressure ($P_b(g)$ per Figure 17, upward force = 30.7 kN)⁴ producing compression in the springs at the top and tension in the springs at the bottom. Under the net loading, the springs in compression at the top resist the difference ($= 1.7 \text{ kN}$) between the weight of the assembly ($= 29 \text{ kN}$) and the (buoyant) force due to hydrostatic pressure ($= 30.7 \text{ kN}$), and the springs in tension at the base of the vessel provide negligible resistance.

The state of the finite element model for net loading under gravity and hydrostatic pressure (i.e., the reflector-block assembly floating inside the vessel but bearing against the head) can be used as the initial condition for dynamic analysis involving three-directional inputs. Herein, the finite element model is used to study the behavior of the assembly in two steps. A discussion of the behavior under a pure vertical input is presented first followed by a discussion of response under a horizontal input (introduced in the previous section).



(a) force-deformation curve defined for multi-linear springs, k_s denotes stiffness

(b) reflector-block assembly, only three representative springs shown at top and bottom, displacements not to scale

Figure 18. Modelling the reflector-block assembly for three directional inputs

A vertical input acceleration $a_z > -g$ was imposed on the reflector-block assembly and a pressure loading history corresponding to the vertical input, $P_b(a_z)$ per Figure 17, was defined on the base of the assembly; see Figure 19a. Figure 19b presents the assumed vertical loading history: a sinusoid with an amplitude of $0.5g$ and a frequency of 1 Hz. Figure 19c presents the corresponding axial force history at

⁴The upwards (buoyant) force can be calculated as $\rho g A H$, where ρ is the density of water ($= 1000 \text{ kg/m}^3$), A ($= 1.66 \text{ m}^2$) is the area of a circle with a radius equal to the outer diameter of the reflector-block assembly, and H ($= 1.89 \text{ m}$) is the height of water above the base of the assembly.

402 the top of the vessel. Expectedly, the vertical reaction history at the head of the vessel is sinusoidal and
 403 can be calculated as $(W / g - \rho A H)(g + a_z(t))$, where W is the weight of the reflector-block assembly, t
 404 is time, and ρ , H , and A are defined in footnote 4. (If the sinusoid has an amplitude of 1g, the reaction
 405 varies between 0 kN and -3.4 kN.)

406 This analysis approach for vertical input applies for $a_z > -g$ because the reflector-block assembly bears
 407 against the head of the vessel (i.e., springs at the top in the finite element model) only if the vertical
 408 acceleration is greater than $-g$. For $a_z < -g$, the reflector-block assembly rests on the base of the vessel
 409 (in theory)⁵ and the pressure loadings on the base of the assembly per Figure 17 do not apply.

410 Analysis of the model described above for a lateral acceleration can be performed as described earlier, but
 411 adjusted to accommodate the pressure loading $P_b(a_x)$ (per Figure 17) on the base of the assembly, which
 412 is addressed here. A sinusoidal pressure time series, as shown in Figure 20a, was assigned at the base of
 413 the reflector-block assembly. The radial variation of the pressure amplitude was linear per Figure 20b and
 414 a $\cos\theta$ -type variation was assumed around the circumference of the assembly. Expectedly, this pressure
 415 loading resulted in a moment at the top support (see Figure 20c) but no horizontal shearing forces within
 416 the assembly.

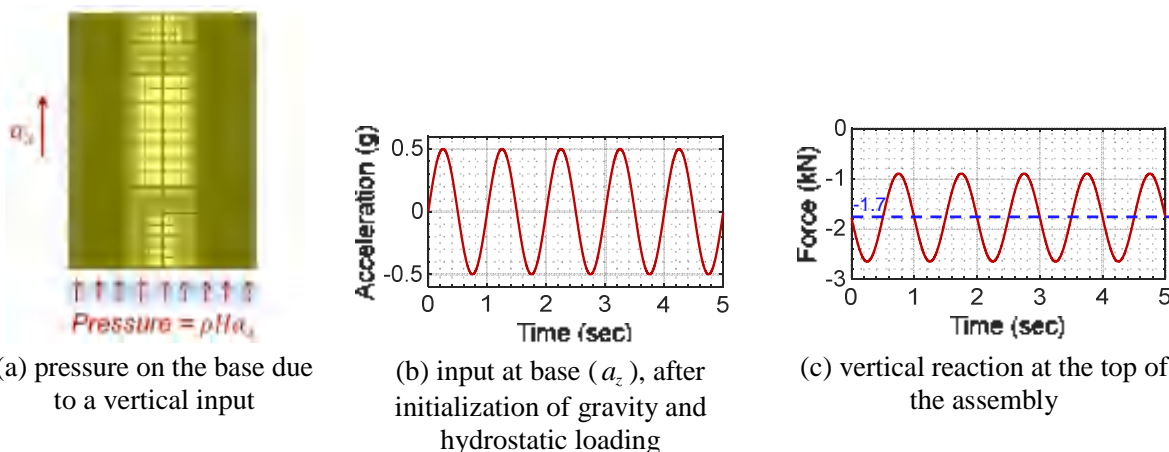


Figure 19. Analysis for a vertical acceleration input ρ is fluid (water) density and H is fluid height above the base of the assembly (= 1.89 m)

417
 418 The load associated with $P_b(a_x)$ per Figure 20b is *transferred* to the top support in the finite element
 419 model as vertical compressive or tensile forces in individual columns of blocks. In the prototype system,
 420 compressive loads would be transferred through block-to-block and block-to-head contact and the tensile
 421 loads would serve only to reduce the compressive load due to hydrostatic pressure and pressure due to the

⁵If the amplitude of the vertical acceleration input is only momentarily smaller than $-g$, the fluid between the base of the vessel and the underside of the assembly may not be able to *quickly* migrate out to allow the assembly to rest on the base of the vessel. However, such high amplitude vertical accelerations could lead to problems in the fluid-flow paths inside the reactor. Hypothetically, if vertical accelerations smaller than $-g$ are sustained for a *significant* duration, the fluid between the base of reflector-block assembly and the base of the vessel will migrate out, allowing the assembly to rest on the base of the vessel. In such a situation, there will be a gap between the top of the reflector-block assembly and the head of the vessel, and it will be filled with fluid.

422 vertical component of ground motion. If the net resultant force on a column due to pressure loading
 423 profiles $P_b(g)$, $P_b(a_z)$, and $P_b(a_x)$ is tensile, the above model is not suitable for estimating shearing
 424 loads between adjacent columns. A column with net vertical tension would move downwards (see
 425 footnote 5) in the prototype system and disengage (i.e., lose contact) from the head, which is similar to the
 426 case of $a_z < -g$ discussed above.

427 In summary, the internal forces in a reflector-block assembly can be analyzed using the modelling
 428 approach described here provided the input accelerations do not lead to its disengagement from the head.
 429 Cases in which a column (or an entire assembly) disengages from the head could be analyzed using finite
 430 element models considering contact and gap elements between blocks. However, such analysis is
 431 unnecessary if the amplitudes of the horizontal and vertical accelerations are small: resulting from siting
 432 the reactor building in a region of low seismic hazard or by implementing seismic isolation. As discussed
 433 in Mir *et al.* (2022b), the implementation of 2D horizontal isolation systems in the tests resulted in
 434 significant reductions in peak horizontal accelerations, particularly for high-intensity seismic inputs (by a
 435 factor of about 4 for the KCE inputs). Vertical and 3D isolation systems, not discussed here (or in Mir *et*
 436 *al.* (2022b)), have been tested and implemented (e.g., Lee and Constantinou (2017), Nawrotzki *et al.*
 437 (2019)), and can be effective in protecting equipment from large vertical accelerations.

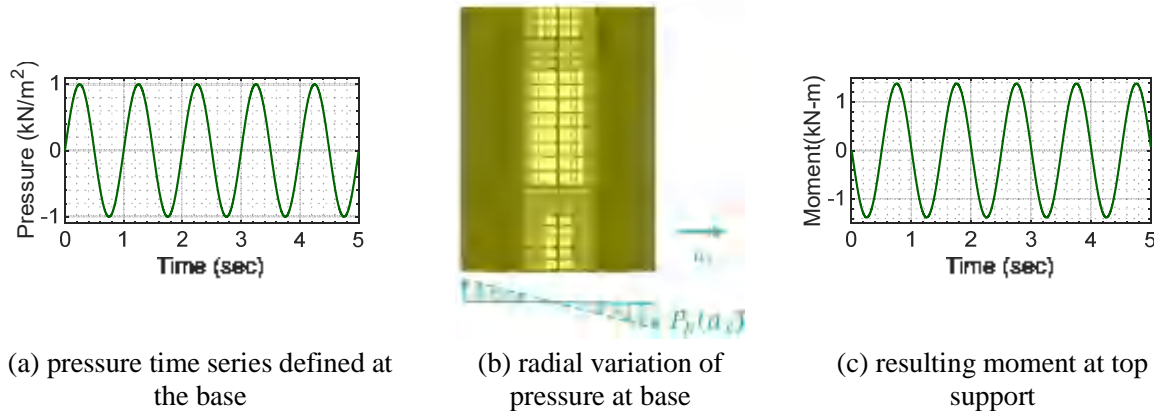


Figure 20. Pressure loading on the base of the reflector assembly, lateral input

438

439 **4. Isolation-system modelling**

440 The modelling of friction pendulum bearings in the finite element package SAP2000 (CSI 2017) is
 441 addressed in this section with the goal of evaluating isolation-system responses (e.g., accelerations above
 442 the isolation plane) that could be used as inputs for estimating responses of components above the
 443 isolation interface. A detailed description of the geometric and mechanical properties of Single Concave
 444 friction Pendulum bearings and Triple Friction Pendulum bearings can be found in literature (e.g., Fenz
 445 and Constantinou (2008)) and is not reproduced here. An SFP bearing has one sliding surface and a TFP
 446 bearing has four sliding surfaces: two inner surfaces and two outer surfaces. The friction at a sliding
 447 surface is characterized by *slow* and *fast* values of the coefficient of friction, which are evaluated at small
 448 and large sliding velocities, respectively. The coefficients of friction on the two inner and the two outer

449 sliding surfaces of a TFP bearing were assumed to be equal. The velocity dependence of the coefficient of
 450 friction at a sliding surface is characterized by a rate parameter (see equation 1 in Mir *et al.* (2022a)). The
 451 vertical stiffness of an SFP or a TFP bearing depends on the imposed load. Table 2 presents the average
 452 properties of the bearings used in the experiments in Mir *et al.* (2022b).

Table 2. Average properties of the bearings used in the earthquake simulator tests in Mir *et al.* (2022b)

	Friction coefficient (%)		Rate parameter (s/cm)	Axial stiffness ($\times 10^5$ kN/m)
	Slow	Fast		
SFP bearings	2.8	10.2	0.44	1.07
TFP bearings [†]	Inner surfaces (2, 3)	2.2	5.1	0.42
	Outer surfaces (1, 4)	6.2	14.3	

[†]The four sliding surfaces of a TFP bearing are numbered 1 through 4. See Mir *et al.* (2022b) for details.

453

454 It was noted earlier that the components of the test specimen including the vessel, core barrel, and the
 455 reflector-block assembly responded as a unit. Accordingly, these components were considered rigid for
 456 the analysis described in this section. Figure 21 presents an isometric view of the model in SAP2000. The
 457 base plate, outer vessel, flange, and the top plate were modelled using rigid shell elements with thickness
 458 per dimensions of the test specimen and a mass density of carbon steel. The mass of the internal
 459 components (reflector assembly, core barrel, water, and pebbles = 3200 kg) was distributed (i.e., lumped)
 460 as an *area mass* on the wall of the vessel. Four isolators (SFP or TFP) were installed under the base plate
 461 at the centers of the green-colored squares in Figure 21.

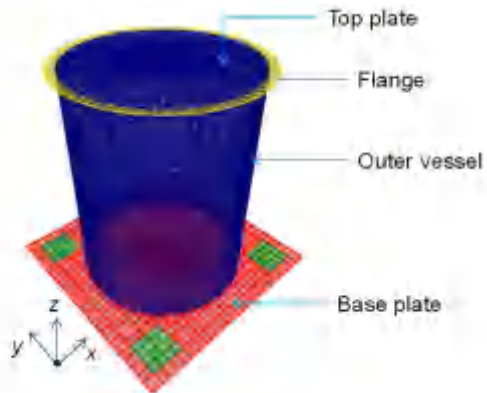


Figure 21. Isometric view of numerical model in SAP2000, and coordinate system

462

463 The *friction isolator* and the *triple pendulum isolator* link elements in SAP2000 were used to model the
 464 SFP and the TFP bearings, respectively. Table 3 and Table 4 presents the key inputs used to define the
 465 force-deformation properties of the two link elements in the axial and the two horizontal directions.
 466 Modal analysis of the finite element model comprising the superstructure introduced in Figure 21 and
 467 four SFP or TFP isolators defined per Table 3 or Table 4, respectively, was performed. Modal frequencies
 468 and mode-shape descriptions are presented in Table 5. As expected, the translational and rocking modes
 469 of the SFP- or TFP- isolated structure were symmetric in the two horizontal directions.

470 Nonlinear response history analyses of the SFP- and TFP-isolated models were performed using
 471 accelerations recorded below the isolation interface in the experiments for the case of two one-directional
 472 (x) inputs (1D CCE-R and 1D KCE per Table 1) and four three-directional inputs (3D CCE, 3D ECE, 3D
 473 KCE and 3D BBM per Table 1). The accelerations recorded below the isolation interface included
 474 rocking and translational components⁶.

Table 3. Key inputs for definition of friction isolator link element in SAP2000

Input field (per SAP2000)	Description
Axial (U1) direction	Effective stiffness for linear or non-linear analysis cases Axial compressive stiffness of the isolator. Value = 1.07×10^5 kN/m per Table 2
	Effective damping for linear analysis case or damping coefficient for nonlinear analysis cases Zero. Damping in the axial direction was defined as modal damping for the vertical mode under load case definition.
Horizontal (U2 or U3) direction	Effective stiffness for linear analysis cases Post-elastic stiffness of the isolator for a given weight. Value = 39.8 kN/m, consistent with a weight per bearing of 18.9 kN and a sliding-surface radius of 0.473 m.
	Effective damping for linear analysis cases Zero. (The response-history analyses were non-linear and so this input is immaterial.)
	Stiffness for nonlinear analysis cases Value = 7868 kN/m: the stiffness of the elastic region of the force-deformation loop, obtained as $\mu_{\max} W / Y$, where μ_{\max} is the maximum (fast) coefficient of friction (see below), W is the weight on the isolator, and Y is the yield displacement of the isolator = 0.3 mm, back-calculated using an experimental-force deformation loop.
	Friction coefficient, fast Value = 12.5%: slightly greater than the 10.2% per Table 2, determined from the from characterization tests. The chosen value of 12.5% better represented the force-displacement behavior observed in earthquake-simulator tests.
	Friction coefficient, slow Value = 3.3%, consistent with value chosen for the coefficient of fast friction and the ratio of fast and slow coefficients of friction per Table 2.
	Rate parameter Value = 44 s/m per Table 2.
	Net pendulum radius Value = 0.473 m per Figure 7a in Mir <i>et al.</i> (2022b).

475
 476
 477
 478
 479
 480

⁶Additional accelerations along/about axes with no specified *command* accelerations were observed due to compliance between the horizontal and vertical actuators of the earthquake simulator. For example, for a 3D input, *command* accelerations were specified along the three translational directions only, but *additional* rotational accelerations about the two horizontal axes were also recorded on the earthquake-simulator platform. This is because actuators in a direction with no *commanded* acceleration are active and experience small motions so as to accommodate the displacements of the actuators along directions with *commanded* accelerations. This is an actuator-related outcome and led to peak accelerations in the three orthogonal directions recorded below the isolation system being greater than the corresponding peak values listed in Table 1.

Table 4. Key inputs for definition of *triple pendulum isolator* link element in SAP2000

Input field (per SAP2000)		Description	
Axial (U1) direction	Effective stiffness for linear or non-linear analysis cases	Axial compressive stiffness of the isolators. Value = 1.05×10^5 kN/m per Table 2.	
	Effective damping for linear analysis case or damping coefficient for nonlinear analysis cases	Zero. Damping in the axial direction was defined as modal damping for the vertical mode under load case definition.	
	Effective stiffness for linear analysis cases	Evaluated as $W / 2R_{eff}$, where W is the weight on the isolator and R_{eff} is the effective radius of the top (or bottom) sliding surface. Value = 21142 N/m. The effective radius R_{eff} is calculated as the difference between the radius of the sliding surface and one-half of the distance between the bottom and top sliding surfaces (height of bearing) and is equal to 0.441 m here.	
	Effective damping for linear analysis cases	Zero (similar to Table 3).	
Horizontal (U2 or U3) direction	Stiffness for nonlinear analysis cases	Outer top and outer bottom	Stiffness before sliding. A reasonably large value, enough to distinguish sliding from not sliding, works well for this input field. Values of 9000 kN/m and 3000 kN/m were used for the outer and inner surfaces, respectively, consistent with the weight on the isolator, the fast friction coefficient of the surfaces (inner or outer) and an assumed yield displacement of 0.3 mm.
		Inner top and inner bottom	
	Friction coefficient, fast	Outer top and outer bottom	Value = 14.3% per Table 2
		Inner top and inner bottom	Value = 5.1% per Table 2
	Friction coefficient, slow	Outer top and outer bottom	Value = 6.2% per Table 2.
		Inner top and inner bottom	Value = 2.2% per Table 2
	Rate parameter		Value = 42 s/m per Table 2
	Radius of sliding surface	Outer top and outer bottom	Value = 0.473 m per Figure 7b in Mir <i>et al.</i> (2022b)
		Inner top and inner bottom	Value = 0.076 m per Figure 7b in Mir <i>et al.</i> (2022b)
	Stop distance	Outer top and outer bottom	Related to the displacement capacity for sliding on the outer surfaces (see Figure 75 in CSI (2017)). Since only a fraction of the displacement capacity of the bearings was used in the tests, a large value (0.5 m) was used here.
		Inner top and inner bottom	Value = 1.27 cm per Figure 7b in Mir <i>et al.</i> (2022b) and Figure 75 in CSI (2017)

Table 5. Summary of modal analysis in SAP2000

Mode number	Description	Frequency	
		SFP-isolated	TFP-isolated
1	Translation along x axis	0.72 Hz	0.52 Hz
2	Translation along y axis	0.72 Hz	0.52 Hz
3	Torsion (rotation about z axis)	0.98 Hz	0.70 Hz
4	Rocking about x axis	29.8 Hz	29.6 Hz
5	Rocking about y axis	29.8 Hz	29.6 Hz
6	Translation along z axis	37.7 Hz	37.5 Hz

484

485 A gravity load case was run initially, the final state of which served as the starting point for the dynamic
 486 analysis. The gravity load case involved *slow* application of acceleration due to gravity as a ramp from 0
 487 to 9.81 m/s^2 in 7 seconds with a large value of modal damping (95% of critical) used to avoid vertical
 488 oscillations. In the response-history analyses, 5% damping was specified for modes 4 through 6 (rocking
 489 and vertical modes). Figure 22 and Figure 23 present numerical and experimental isolation system
 490 responses (acceleration spectra and force-displacement loops) in the SFP- and TFP- isolated cases,
 491 respectively, for the 3D KCE input. Acceleration spectra immediately below (input) and above the
 492 isolation system (i.e., on the base plate) are presented in the figures to enable a comparison. Table 6
 493 through Table 8 present the absolute maximum experimental and numerical values of key isolation-
 494 system responses in the SFP- and TFP- isolated configurations for the 1D and 3D inputs. The agreement
 495 between experimental results and numerical predictions for isolation-system responses is excellent. The
 496 absolute differences between peak experimental and numerical responses in the SFP- (TFP-) isolated case
 497 are less than 7%, 4%, 11%, and 24% (8%, 6%, 17%, and 11%) on average for isolator displacements,
 498 reaction forces, horizontal accelerations, and vertical accelerations, respectively. The shapes of the
 499 rocking acceleration response spectra are captured reasonably well using the numerical model. However,
 500 hard-to-characterize differences in damping in the rocking modes (and in the vertical mode⁷) do exist
 501 between the experimental specimen and the numerical model.

502 The accuracy of the numerical results obtained from the SFP-isolated and the TFP-isolated models
 503 indicate that utilizing a *rigid superstructure with lumped internal mass* is sufficient for obtaining accurate
 504 isolation-system responses.

505

⁷At the time of this writing, the element for the friction pendulum bearing in SAP2000 does not track the change in height of the isolator as a function of its horizontal relative displacement.

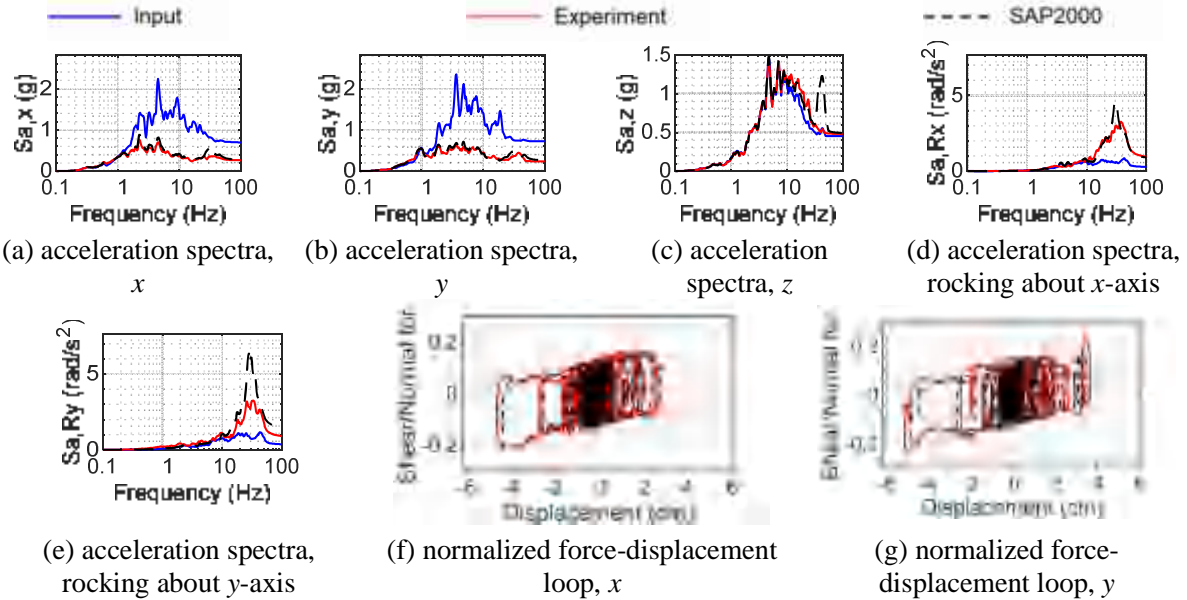


Figure 22. Numerical and experimental results, isolation-system responses, 3D KCE motion, SFP-isolated configuration, acceleration spectra for 5% damping

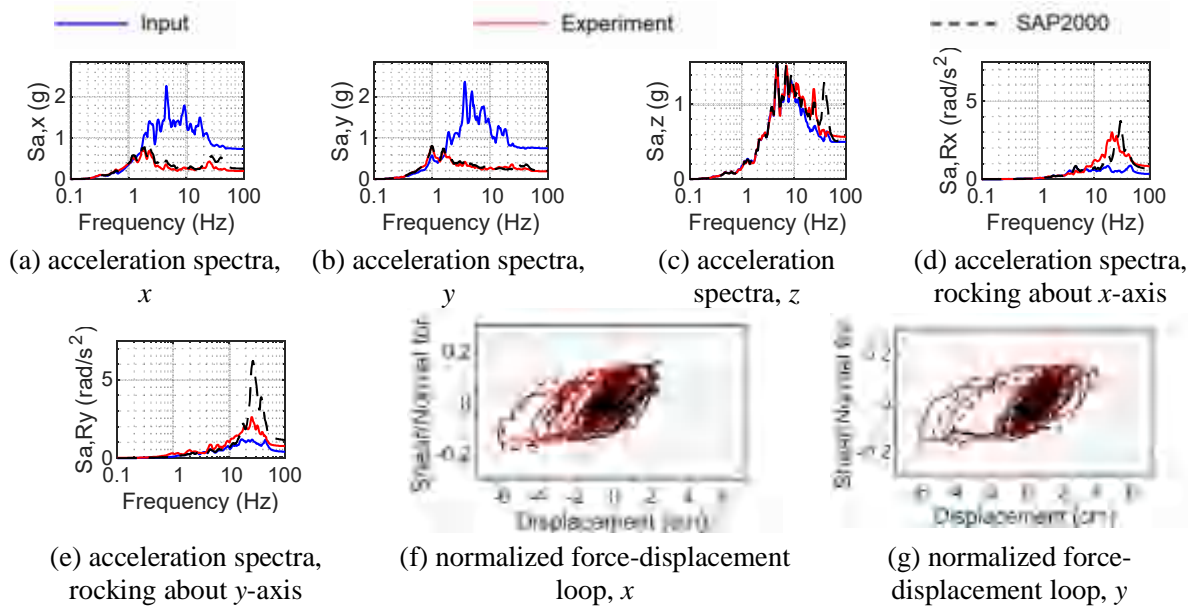


Figure 23. Numerical and experimental results, isolation-system responses, 3D KCE motion, TFP-isolated configuration, acceleration spectra for 5% damping

Table 6. Maximum absolute isolation-system responses and percentage differences, 1D inputs

Response	SFP-isolated						TFP-isolated					
	1D CCE-R			1D KCE			1D CCE-R			1D KCE		
	Model	Exp.	Diff., %	Model	Exp.	Diff., %	Model	Exp.	Diff., %	Model	Exp.	Diff., %
Isolator displacement, x , cm	3.4	3.2	7	3.1	3.3	-6	5.8	5.8	0	5.8	5.6	3
Shear force, x , kN	14.6	14.3	3	13.8	14.8	-6	14.3	13	10	14	12.8	10
Normal force, kN	78.9	77.0	2	80	77.6	3	77.8	80.1	-3	79.4	83.4	-5
Acceleration, x , g	0.21	0.18	16	0.23	0.18	28	0.21	0.17	24	0.19	0.16	22

Table 7. Maximum absolute isolation-system responses and percentage differences, 3D inputs, SFP-isolated configuration

Response	3D CCE-R			3D ECE			3D KCE			3D BBM		
	Model	Exp.	Diff., %	Model	Exp.	Diff., %	Model	Exp.	Diff., %	Model	Exp.	Diff., %
Isolator displacement, x , cm	3.5	3.6	-2	2.2	2.3	-6	4.3	4.6	-6	1.3	1.3	-4
Isolator displacement, y , cm	0.8	0.9	-14	2.4	2.5	-4	4.8	5.1	-6	0.8	0.9	-11
Shear force, x , kN	15.4	15.0	3	12.8	13.2	-3	19.3	19.8	-3	11.8	12.0	-2
Shear force, y , kN	9.8	10.7	-8	14.0	13.3	5	17.8	17.6	1	9.9	10.1	-3
Normal force, kN	92.8	86.9	7	92.1	92.4	0	103.4	105.4	-2	92.2	94.1	-2
Acceleration, x , g	0.21	0.18	12	0.19	0.17	16	0.28	0.26	6	0.20	0.21	-4
Acceleration, y , g	0.13	0.13	1	0.18	0.17	8	0.26	0.23	13	0.13	0.13	1
Acceleration, z , g	0.27	0.15	82	0.32	0.34	-6	0.49	0.47	3	0.26	0.26	-2

Table 8. Maximum absolute isolation-system responses and percentage differences, 3D inputs, TFP-isolated configuration

Response	3D CCE-R			3D ECE			3D KCE			3D BBM		
	Model	Exp.	Diff., %	Model	Exp.	Diff., %	Model	Exp.	Diff., %	Model	Exp.	Diff., %
Isolator displacement, x , cm	6.5	6.3	2	3.2	3.7	-14	5.9	6.1	-3	3.6	3.4	5
Isolator displacement, y , cm	1.5	1.8	-14	3.5	3.8	-7	5.2	5.9	-13	2.2	2	10
Shear force, x , kN	15.5	13.6	14	12.3	12.5	-2	16.6	14.7	13	12.1	11.6	5
Shear force, y , kN	10.7	10.4	3	13.4	12.9	3	15.5	14.6	6	8.6	7.9	9
Normal force, kN	89.5	89.4	0	90.5	93.5	-3	106.4	104.9	1	99.4	101.5	-2
Acceleration, x , g	0.22	0.18	21	0.19	0.16	14	0.25	0.2	28	0.19	0.16	16
Acceleration, y , g	0.16	0.14	14	0.2	0.18	8	0.2	0.19	6	0.12	0.1	17
Acceleration, z , g	0.23	0.18	27	0.3	0.31	-3	0.5	0.56	-10	0.36	0.38	-4

5. Closing remarks

A molten salt reactor that uses spherical fuel pebbles and positively buoyant graphite blocks as moderator is at an advanced stage of development at the time of this writing. Seismic isolation is being considered in the design of the reactor to support rapid deployment at sites of very different seismic hazard. Data and observations from an earthquake-simulator testing program conducted on a scaled model of the reactor were used in this paper to formulate recommendations for seismic analysis of the reactor's components. The focus of this paper was on the seismic behavior of the fluid (coolant) in the thin annular spaces inside the reactor vessel, the estimation of internal seismic forces in the reflector-block assembly, and evaluation of isolation system responses. Recommendations are summarized below and apply to molten salt and liquid metal reactor vessels with similar fluid-structure geometries.

1. *Fluid behavior*: Numerical simulation of sloshing wave height responses in small annular spaces is challenging in terms of computational cost and the uncertainty associated with defining fluid- and geometry-specific damping in sloshing modes inside the annuli. The *double annulus*, fluid-only model described in this study can be used to estimate hydrodynamic pressure histories for analysis of structural and mechanical components inside the reactor vessel.
2. *Internal forces in a reflector-block assembly*: The preliminary design of connectors in a reflector-block assembly can be performed using the approach presented in this paper. Final design should address construction tolerances between the connectors and the blocks. Under extreme vertical and horizontal seismic inputs, dynamic fluid loadings on the reflector-block assembly may lead it to disengage from the head of the vessel, disrupting load paths and affecting fluid-flow paths inside the reactor vessel. Horizontal and vertical seismic isolation can substantially mitigate the effects of extreme earthquake shaking of a reactor vessel and its internals, permitting simpler design solutions and allowing the design approaches described in this paper to be used.
3. *Base-isolation systems*: Two horizontal isolation systems utilizing Single concave Friction Pendulum bearings and Triple Friction Pendulum bearing were studied. Accurate estimates of isolation-system responses were obtained by analysis of a rigid vessel, with the mass of the internal components and fluid distributed over the area of its wall, and specific link elements, representing the isolators, in the finite element package SAP2000.

6. Acknowledgements

The information, data, or work presented herein was funded by the Advanced Research Projects Agency-Energy (ARPA-E), U.S. Department of Energy, under Award Number DE-AR0000978. Kairos Power contributed knowledge and hardware for the experiments. The views and opinions of the authors expressed herein do not necessarily state or reflect those of the United States Government or any agency thereof, or Kairos Power. The authors thank Brian Song, Matthew Clavelli, Oded Doron and Per Peterson of Kairos Power, Kaniel Z. Tilow of Simpson Gumpertz & Heger (Atlanta), Mark Pérès of Peres Engineering, and Kaivalya M. Lal of the University at Buffalo for providing input to this study. Earthquake Protections Systems contributed the seismic isolators. Computers and Structures Inc. provided

a SAP2000 license to support remotely-executed numerical analyses presented in this paper. The authors thank the technical staff in the Structural Engineering and Earthquake Simulation Laboratory at the University at Buffalo for their assistance in fabricating and instrumenting the test article and executing the experiments.

7. References

- CSI. (2017). "CSI analysis reference manual." Computer and Structures, Inc., Berkeley, CA, USA.
- DOE. (2019). "TRISO particles: the most robust nuclear fuel on earth." United States Department of Energy, Washington, D.C.
- Fenz, D. M., and Constantinou, M. C. (2008). "Mechanical behavior of multi-spherical sliding bearings." *Report MCEER-08-0007*, The State University of New York at Buffalo, Buffalo, NY.
- Lee, D., and Constantinou, M. C. (2017). "Development and validation of a combined horizontal-vertical seismic isolation system for high-voltage-power transformers." *Report MCEER-17-0007*, The State University of New York at Buffalo, Buffalo, NY.
- Livermore Software Technology Corporation (LSTC). (2017). "LS-DYNA user's manual – Version R 11.0." Livermore Software Technology Corporation, Livermore, CA, USA.
- Mir, F. U. H., Lal, K. M., Whittaker, A. S., and Constantinou, M. C. (2022a). "Validation of a numerical model of a seismically isolated, cylindrical, fluid-filled vessel." *Earthquake Engineering & Structural Dynamics*, 51(8), 1857-1873.
- Mir, F. U. H., Whittaker, A. S., Kosbab, B. D., and Nguyen, N. (2022b). "Characterizing the seismic response of a molten salt nuclear reactor." *Earthquake Engineering & Structural Dynamics*, 52(7), 2025-2046.
- Mir, F. U. H., Yu, C.-C., Whittaker, A. S., and Constantinou, M. C. (2022c). "Physical and numerical simulations of fluid-structure interaction in advanced nuclear reactors" *Report MCEER-22-0002*, The State University of New York at Buffalo, Buffalo, NY.
- Nawrotzki, P., Siepe, D., and Salcedo, V. (2019). "Seismic protection of NPP structures by 3-D base control systems." *Transactions, 25th International Conference on Structural Mechanics in Reactor Technology (SMiRT-25)*, Charlotte, NC.
- Tang, Y., Grandy, C., and Seidensticker, R. (2010). "Seismic response of annular cylindrical tanks." *Nuclear Engineering and Design*, 240(10), 2614-2625.
- Veletsos, A. S. (1984). "Seismic response and design of liquid storage tanks." *Guidelines for the seismic design of oil and gas pipeline systems*, Committee on Gas and Liquid Fuel Lifelines, American Society of Civil Engineers (ASCE), Reston, VA, 255-370.
- Yu, C.-C., and Whittaker, A. S. (2021). "Analytical and numerical studies of fluid-structure interaction in liquid-filled vessels - revision 1." *Report MCEER-20-0003*, The State University of New York at Buffalo, Buffalo, NY.
- Yu, C.-C., and Whittaker, A. S. (2022). "A process to verify numerical models for seismic fluid-structure interaction in advanced reactor vessels." *Nuclear Engineering and Design*, 387, 111580.